

FUELCELL2009-85092

A NOVEL APPROACH TO CHARACTERIZE MICRO POROUS LAYER - CATALSYT LAYER INTERFACE STRUCTURE IN POLYMER ELECTROLYTE

FUEL CELLS

F. E. Hizir¹, T. Swamy¹, S. O. Ural², E. C. Kumbur¹, and M. M. Mench¹

¹ Penn State Fuel Cell Dynamics and Diagnostics Lab
Department of Mechanical and Nuclear Engineering
Penn State University, University Park, PA 16802 USA

²Materials Sience and Engineering Department
Penn State University, University Park, PA 16802 USA

*Corresponding Author's e-mail: mmm124@psu.edu

ABSTRACT

The impact of interfacial contact between the catalyst layer (CL) and diffusion medium (DM) has important implications for the transport of heat, current, and multi-phase flow in the membrane electrode assembly. This work is motivated by the need to obtain a greater understanding of the impact of the micro porous layer (MPL) and CL morphologies and resulting interfacial contact on the fuel cell performance. In this effort, an array of different virgin mating CL and MPL surface structures was investigated. The mating surface morphology of the tested MPL and CL samples were digitally characterized by Optical Profilometry (OP), a unique non-destructive imaging technique, which allows for obtaining the 3-D surface topology of samples with a resolution of on the order of several nanometers in the vertical direction and 0.5 to 5 microns in the lateral direction. The benchmark data were further utilized in an analytical model developed for virtual reconstruction of a realistic interfacial structure. The results show that the MPL surface exhibits a higher degree of roughness compared to catalyst surfaces. Crack size and locations on the surface vary for both samples;

however, the cracks on the MPL surface are observed to have relatively higher amplitude than similar structures on the CL, indicating the possibility of dominance of the MPL surface morphology on the local transport across the MPL|CL interface. Further investigations are underway to understand the impact of the interfacial morphology and material properties on capillary flow and interfacial electronic and thermal resistance at MPL-CL interface.

Keywords: PEFC, MPL, CL, GDL, interface, morphology, contact resistance, water transport.

1. INTRODUCTION

Fuel cells are a promising and rapidly expanding power technology with a broad range of potential applications. Specifically, polymer electrolyte membrane (PEM) fuel cells have aroused growing interest, because of their low operation temperature, quick start up and low emission characteristics. This increasing interest requires that the fuel cell performance be enhanced, and that the fuel cell be made more energy efficient. The

performance of the fuel cell is dictated by the polarization characteristics of it which leads to a departure from the ideal voltage. The polarization behavior is a result of three types of phenomena: electrode kinetic losses, ohmic losses and mass transport losses. Among these losses, mass transport and specifically water transport losses present a big challenge and require a better understanding in order to design a more efficient fuel cell stack [1-3]. It has also been observed that the ohmic losses are dominant at normal fuel cell operating conditions and hence require considerable attention. A major source of losses originates at the interfaces between the various components of the fuel cell and in this study; we focus on the micro porous layer (MPL) and the catalyst layer (CL) interface.

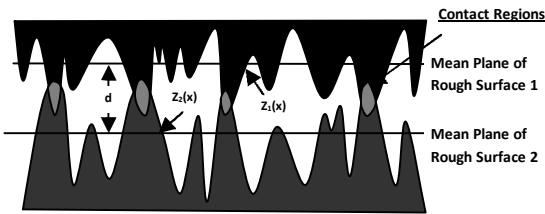


Figure 1. Schematic of the contact between 2 rough surfaces

It has been observed that all surfaces are inherently rough at the microscopic level (figure 1) which results in the following issues at the interface between two mating surfaces, such as the MPL/CL interface in a fuel cell:

1. There is a considerable loss in contact area leading to electrical and thermal contact resistances.
2. There are interfacial gaps created where the surface profiles do not mate.

Hence, the MPL/CL interface and the issues associated with it require a better understanding in order to estimate the resulting interfacial losses and their effect on the fuel cell performance.

A lot of work has been done that focuses on mass transport losses in a fuel cell. Some of these studies present a dedicated analysis on the impact of CL [4-8] and MPL [9-15] on mass transport. Also, among a variety of experimental studies that quantify the various interfacial resistances that exist in a fuel cell [ref], only a few have made an attempt to identify the MPL/CL interfacial resistance in particular [ref]. However, none of the studies done so far have examined the MPL/CL interfacial morphology to understand its effect on the interfacial resistance and possible mass transport losses, which originate at the MPL/CL interface.

Some notable work has been done to model the gas diffusion layer (GDL) and bipolar plate (BPP) interface [16,17] in order to estimate the contact resistance but, no efforts have been made to model the MPL/CL interfacial resistance based on the morphology of the mating surfaces. It must also be noted that interfacial resistance modeling based on surface morphologies has been dealt extensively in the field of electrical contact mechanics and tribology [18-24]. These micro-contact models are based on the stochastic nature of the asperities on the surfaces in contact and hence employ statistical analysis to estimate their interfacial resistance. Among the most widely used models, the Greenwood and Williamson's (GW) model [19], with its parameters evaluated using Nayak's [21] statistical techniques, provide us with the required basis to mathematically reconstruct an interface between two surfaces. Also, Holm's [25] valuable work gives us the necessary background that helps us evaluate the interfacial resistance at a micro-level, making it possible for integration with GW model. It must be pointed out that since these statistical approaches depend on the surface profile characteristics and material properties but not directly on the type of material, the application of these models to the MPL/CL interface seems viable.

So, in this study we focus on the digital characterization of the surface topology of the MPL/CL interfacial structure in order to understand its effect on the interfacial mass transport and contact resistance losses. We also present a model that directly utilizes the morphological data of the mating surfaces to predict the contact resistance losses arising at the MPL/CL interface.

2. EXPERIMENTAL PART

To characterize the MPL/CL interfacial morphology, surface structures of different MPL and CL samples were investigated separately. Among a number of techniques developed to study surface topography, optical profilometry was used to quantify surface roughness and morphology of the samples. Implementation of this non-contact method in the measurements avoided surface damage, and hence erroneous measurements of the roughness profiles of the samples [26]. However, surfaces that reflect light poorly or disperse it, like for instance MPL and CL surfaces cannot be measured properly using optical profilometry [27]. Certain parts of the profilometry data, a matrix of data points that enables quantitative roughness and height measurements, will be missing for specimens with such surface characteristics. This

problem can partly be solved by sputtering the surface with a thin layer of gold. The layer thickness needs to be optimized to avoid the sputter process introducing an artificial roughness to the surface and damaging it [28, 29].

A measurement procedure consisting of two steps was designed to determine the optimum gold coating thickness required to perform optical profilometry measurements of MPL and CL surfaces. In step 1, samples sputtered for different amounts of time were scanned using optical profilometry. Images obtained were compared to determine the gold sputtering time that is sufficient to get good enough profilometry data with minimum number of missing data points. In step 2, effects of increasing gold coating thickness on the surface morphology of the samples were investigated. Because surface topology of MPL and CL is highly variable, changes in the morphology due to sputtering can only be determined by examining the exact same region on the sample surfaces before and after sputtering. It is a difficult task to scan exactly the same location on a specimen using tools such as AFM or optical profilometry which would allow for quantitative measurements. Therefore, SEM images of the same regions on the specimen surfaces were compared after different durations of sputtering were applied. Combining results of step 1 and 2, optimum sputtering time that would yield sufficiently complete profilometry data with minimal changes in the surface morphology was obtained.

2.1 Materials:

Naturally cracked catalyst layer (GORE™ Primea Series 57 MEA) and MPL side of carbon felt type diffusion media (SGL 10BB) were used in determination of the optimum sputtering time. Optical profilometry measurements were performed on artificially cracked catalyst layer (supplied by W.L Gore) and MPL side of SLG 10 BB sputtered for the optimum time (Figure 2). Material properties of SGL 10BB supplied by the manufacturer are summarized in Table 1. No information is available regarding the properties of cracked catalyst layer supplied by manufacturer.

2.2 Equipment:

Gold sputtering was performed in a Balzers SCD 050 Sputter Coater with a plasma current of 25 mA, a working distance of 30 mm, and at an Argon pressure of 30 Pa.

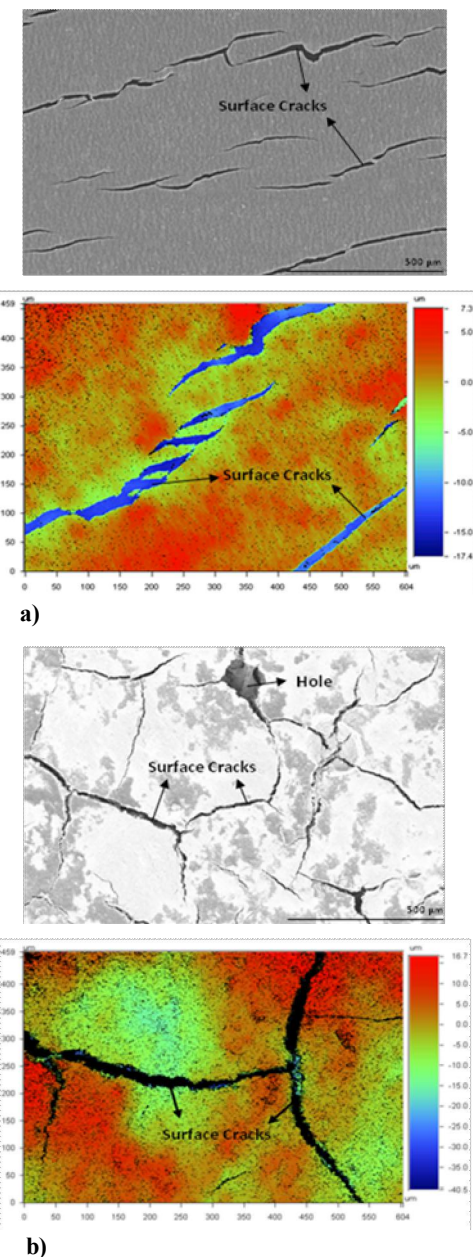


Figure 2. SEM and optical profilometry images of a) cracked catalyst layer, b) MPL side of SGL 10BB

Optical profilometry measurements were performed using a Wyko NT100 optical profilometer in VSI mode. The resolution in z-direction was approximately 3 nm, and the scanned areas were 598 μm x 454 μm in size with a sampling interval of 0.82 μm in x-direction and 0.95 μm in y-direction.

SEM images of the samples were taken using a Hitachi S-3000H scanning electron microscope.

Properties	Unit	Value
Thickness	µm	420
Areal weight	g/m ²	125
Porosity	%	84
Air Permeability	cm ³ /cm ² .s	3
Electrical resistance (through plane)	m.Ω.cm ²	< 15
Existence of MPL		Yes

Table 1. Material properties of SGL 10BB

2.3 Determination of Optimum Sputtering Time for Naturally Cracked Catalyst Layer

In step 1 of the measurement procedure, 6 different CL samples that were approximately 1 cm x 1 cm in size were cut using a razor blade. The samples were fixed on SEM stubs using double-sided adhesive conductive carbon pads, and sputtered with gold for 40 seconds, 1 minute, 2 minutes, 3 minutes, 4 minutes and 6 minutes, respectively. Arbitrary areas were scanned on each sample using optical profilometry. Two dimensional optical profilometry images of the scanned areas are shown in Figure 3. Number of black points on the images (representing missing data points due to low reflectivity and high surface roughness) decrease dramatically with increasing sputtering time till 4 minutes of sputtering is reached. For sputtering times longer than 4 minutes, a significant improvement in optical profilometry images is not observed. Hence, 4 minutes of sputtering is concluded to be sufficient to get satisfactory optical profilometry images of the CL with a reasonable amount of missing data.

In the second part, a single CL sample that was approximately 1 cm x 1 cm in size was cut using a razor blade. The sample was fixed on an SEM stub using a double-sided adhesive conductive carbon pad. First SEM images of a specific region on the CL specimen were captured without any sputtering. Then SEM images of the exact same region were taken after the same specimen was sputtered for 2 minutes, 3 minutes and 4 minutes in total by the application of a series of sequential sputtering processes. SEM images obtained indicated a small growth in surface particle size and a small decrease in surface pore size which is less than 0.05 µm for sputtering times less than or equal to 4 minutes (Figure 4 b, c, d) compared to the virgin case (Figure 4 a).

Comparing results of step 1 and 2, optimum sputtering time to perform optical profilometry measurements of catalyst layer was determined as 4

minutes, since a 0.05 µm change in the surface morphology of CL due to 4 minutes of sputtering is not significant.

2.4 Determination of Optimum Sputtering Time for MPL Side of SGL 10BB

Same measurement procedure used for CL is applied to MPL. In the first part, optical profilometry images of 5 different MPL samples, a virgin sample and samples sputtered for 4 minutes, 5 minutes, 6 minutes and 7 minutes, were captured (Figure 5). Optical profilometry data regarding crack depth was observed to be completely missing independent of the sputtering time, as can be seen from the completely black structures representing cracks in Figure 5. However, missing data from the remaining portions of the surface (corresponding to the black spots spread over the images in Figure 5) was observed to decrease with increasing sputtering time. By comparing the images, 6 minutes of sputtering was concluded to be sufficient to get satisfactory optical profilometry data from the MPL.

In the second part, SEM images of the same location on an MPL sample were captured without any sputtering, and after sputtering the sample for 2 minutes, 4 minutes, 6 minutes and 11 minutes in total (Figure 6). For sputtering times less than or equal to 6 minutes, no changes were observed in the SEM images captured (Figure 6 a, b, c, d). For 11 minutes of sputtering, surface morphology of MPL was observed to change greatly. SEM images indicated a growth in particle size which was around 0.5 µm and some of the pores on the surface were observed to disappear. Comparing results of step 1 and 2, optimum sputtering time to perform optical profilometry measurements of MPL was determined as 6 minutes.

2.5 Optical Profilometry Measurements

Optical profilometry measurements were performed for 18 different locations on MPL and cracked CL surfaces after applying 6 minutes and 4 minutes of sputtering, respectively. Measurement locations were selected to be uniformly distributed over the entire surfaces in the form of a 6 x 3 matrix.

2.6 SEM Measurements

To have a better understanding of the surface characteristics of the samples, additional SEM images of virgin MPL and cracked CL surfaces were taken at higher working distances.

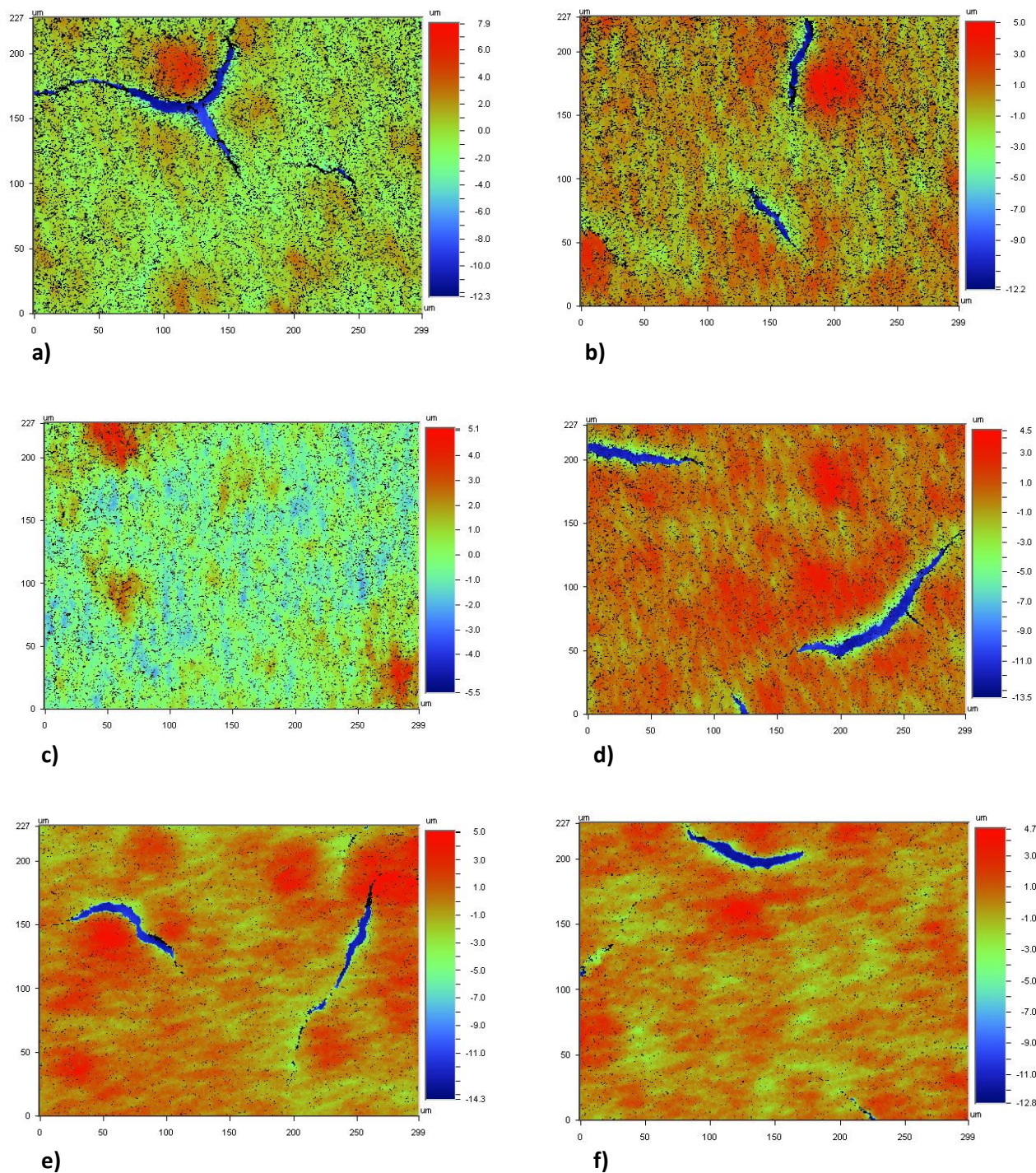
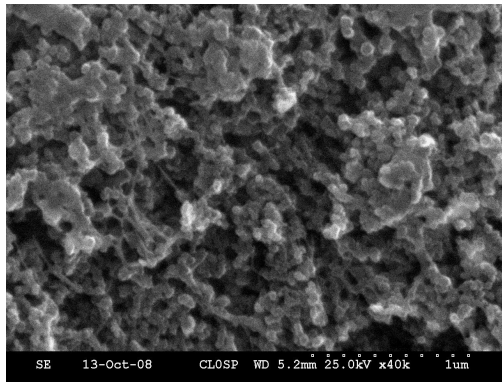
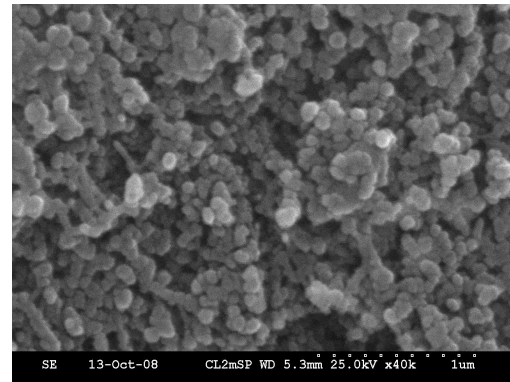


Figure 3. 2D Optical profilometry images of naturally cracked catalyst layer after a) 40 seconds of sputtering, b) 1 minute of sputtering, c) 2 minutes of sputtering, d) 3 minutes of sputtering, e) 4 minutes of sputtering, f) 6 minutes of sputtering.



a)

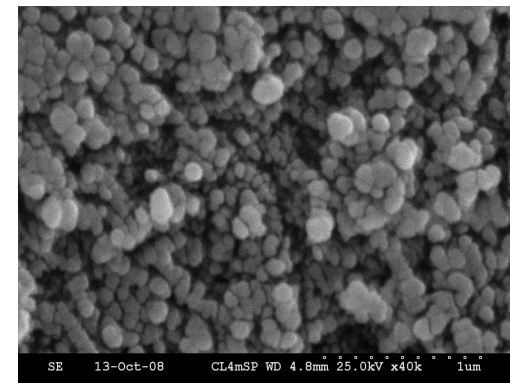
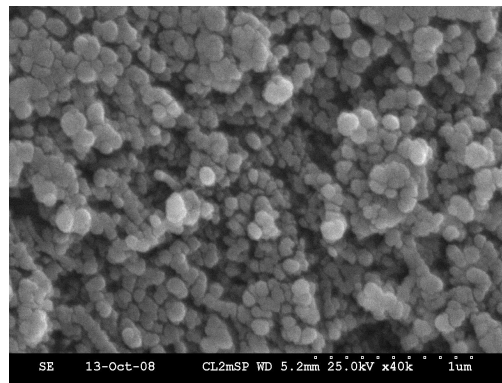


b)

c)

d)

Figure 4. SEM Images of naturally cracked catalyst layer a) without any sputtering, b) after 2 minutes of sputtering, c) after 3 minutes of sputtering, d) after 4 minutes of sputtering.



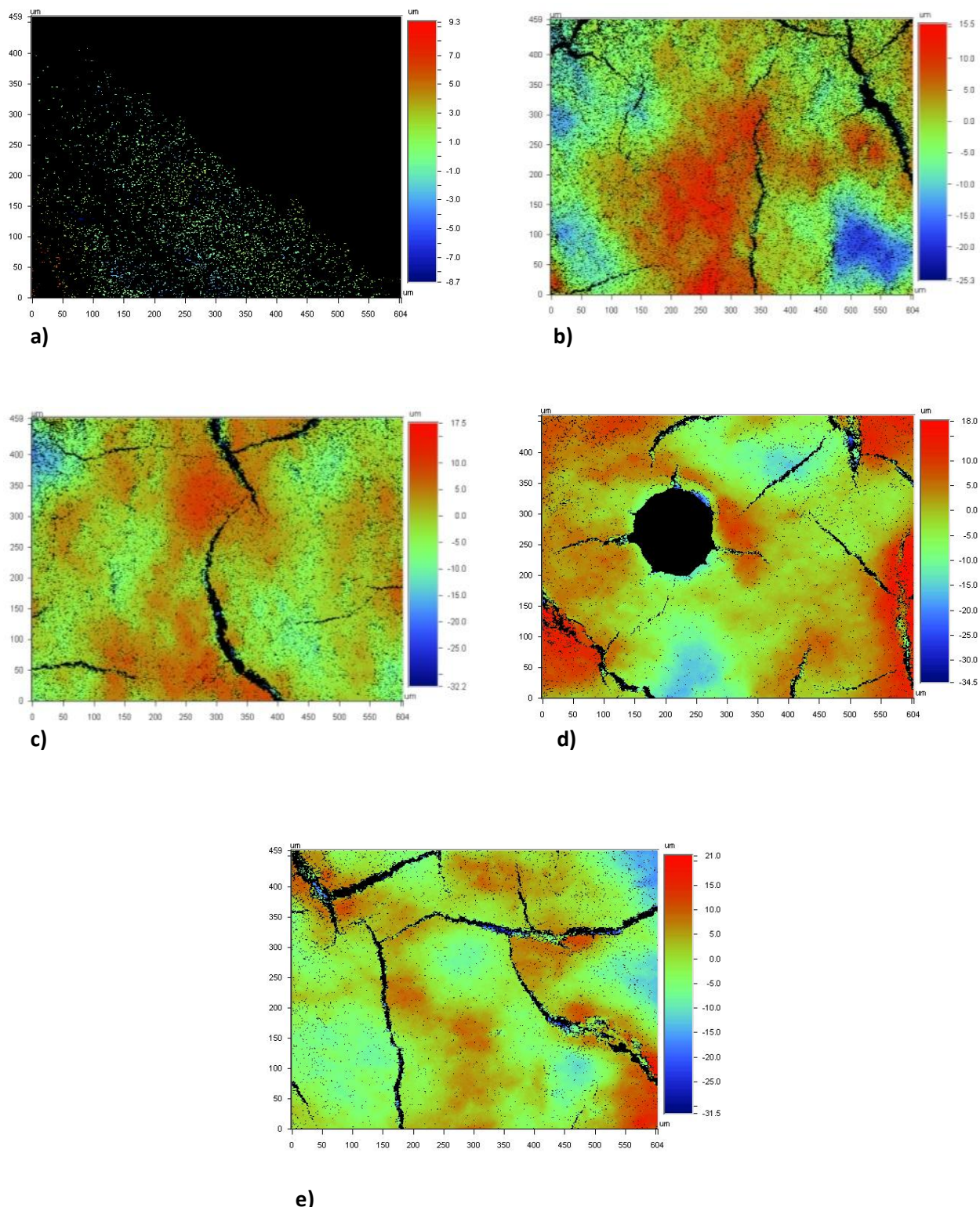
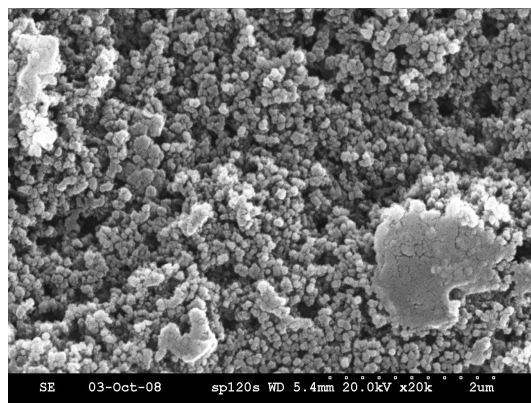
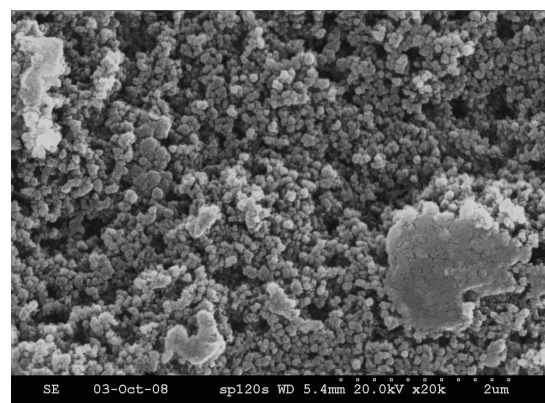


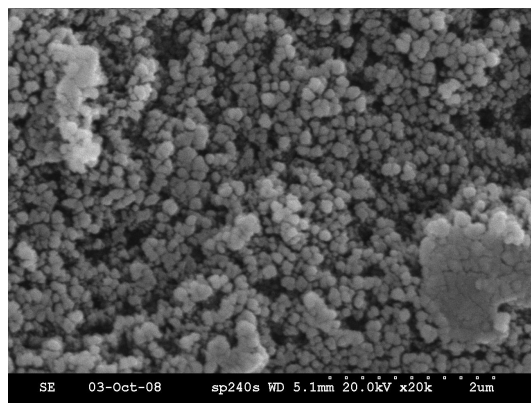
Figure 5. 2 dimensional optical profilometry images of MPL side of SGL 10BB a) without any sputtering, b) after 4 minutes of sputtering, c) after 5 minutes of sputtering, d) after 6 minutes of sputtering, e) after 7 minutes of sputtering.



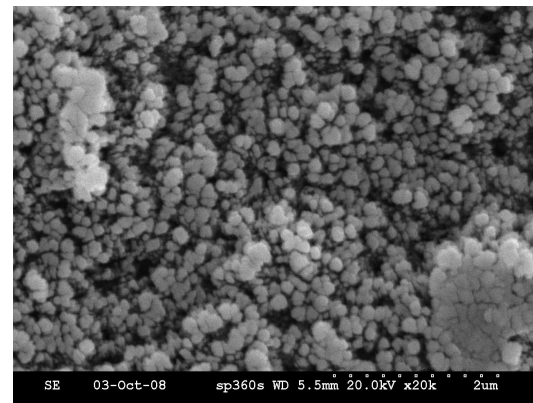
a)



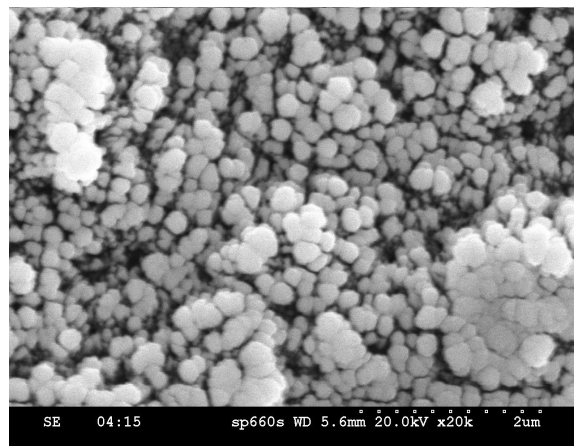
b)



c)



d)



e)

Figure 6. SEM Images of MPL side of SGL 10BB a) without any sputtering, b) after 2 minutes of sputtering, c) after 4 minutes of sputtering, d) after 6 minutes of sputtering, e) after 11 minutes of sputtering.

3. MPL/CL INTERFACIAL RESISTANCE MODEL

As mentioned in the introduction we employ the GW model [19] as our basic framework to reconstruct the interface between the MPL and CL surfaces. It was also mentioned that the parameters required in the GW model can be evaluated statistically, as shown by Nayak [21]. In order to obtain these parameters for the MPL and CL surfaces, we first develop a continuous mathematical representation of the discrete surface profile data of the two surfaces, obtained using optical profilometry. This task is accomplished by using the Discrete Fourier Transform (DFT), which generates a continuous representation of the discrete data as a sum of sine and cosine terms or correspondingly, in their complex notation (figure 7). Since 3-D surfaces require exorbitant computational time for parameter evaluation, as an approximation, we choose typical cross-sections of the discrete surface profile data and feed them to the DFT algorithm.

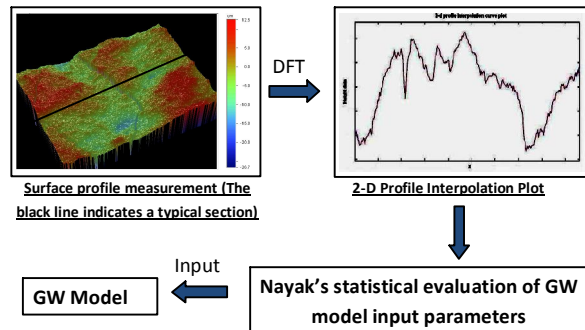


Figure 7. Profile data processing technique

The DFT algorithm is applied to the discrete data $z(x)$, in the following manner:

$$C(j) = \sum_{n=1}^N z(n) e^{-\frac{2\pi i(n-1)(j-1)}{N}} \quad (1)$$

Where, $C(j)$ represents the Fourier coefficients. N represents the number of discrete data points in each profile considered. The continuous analytical representation $Z(x)$ is thus obtained as:

$$Z(x) = \frac{1}{N} \sum_{n=1}^N C(n) e^{-\frac{2\pi i(n-1)(x-1)}{N}} \quad (2)$$

The above algorithm is implemented on both, MPL and CL data to obtain continuous representations $Z_{MPL}(x)$ and $Z_{CL}(x)$ respectively.

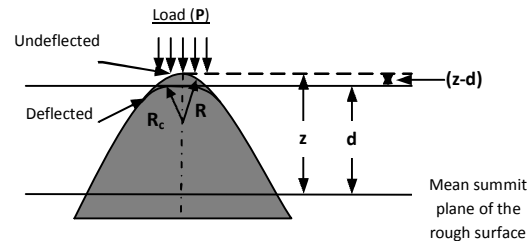


Figure 8. Contact geometry at summits

It is clear that the MPL and CL surfaces, just like any other surface, are inherently rough (figure 1) with asperities distributed randomly over the entire surface. At this stage, we approximate the MPL/CL contact to be elastic and asperity interactions on the same surface are neglected under normal operating conditions of the fuel cell. In order to apply the GW model to the MPL/CL interface, we first develop a model for the contact between a rough and a smooth surface. According to the Hertzian theory [18, 19] of elastic contact, the load P on a single summit (figure 8) of height z radius R can be evaluated as

$$P = \frac{4}{3} E_{eq} R^{\frac{1}{2}} (z - d)^{\frac{3}{2}} \quad z > d \quad (3)$$

$$E_{eq} = \left[\frac{1 - v_1^2}{E_1} + \frac{1 - v_2^2}{E_2} \right]^{-\frac{1}{2}} \quad (4)$$

Where, v_i and E_i ($i = 1, 2$) are the Poisson's ratio and Young's modulus of the two materials in contact, Eq. (4) representing the effective Young's modulus as E_{eq} . Also, approximating current flow is independent due to the large separation between asperities; R. Holm [25] gives the electrical contact conductance for a single contact as in figure 3 to be

$$g_c = \frac{4R_c}{\rho_1 + \rho_2} \quad (5)$$

$$R_c = \sqrt{R(z - d)} \quad (6)$$

Where, ρ_i ($i = 1, 2$) is the electrical resistivity of the materials in contact (MPL and CL) and R_c is the deformed contact radius of the summit as shown in figure 3.

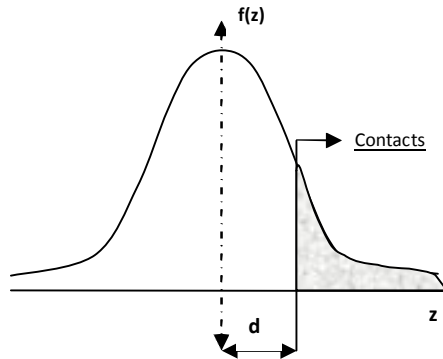


Figure 9. Gaussian distribution of summit heights

To extend the theory to the entire surface encompassing all the asperities, we consider certain statistical parameters that describe the rough surface and incorporate them into Eq. (3), which is then integrated over the whole surface. For the given rough surface, we approximate that its randomly distributed asperities are all spherical in shape with a constant radius R , and have a Gaussian probability distribution (figure 9) with σ_{sum} as the standard deviation of the summits. Also, let the density of summits on the surface be D_{sum} . The probability density function can be defined as

$$f(z) = \frac{1}{\sigma_z \sqrt{2\pi}} e^{-\frac{z^2}{2\sigma_{sum}^2}} \quad (7)$$

Now, the probability that a randomly selected summit has a height in excess of d is

$$p(z > d) = \int_d^\infty f(z) dz \quad (8)$$

It is clear that the load P is a function of the random variable z . The average value of function of a random variable is obtained by integrating the product of the function in consideration and the probability density of the random variable over the domain of the random variable. Hence, averaging P over the entire surface and dividing by the nominal area, we obtain the compression pressure p to be

$$p = \int_d^\infty \frac{4}{3} E_{eq} D_{sum} R^{\frac{1}{2}} (z - d)^{\frac{3}{2}} f(z) dz \quad (9)$$

Here, we approximate the compression pressure to be uniform over the fuel cell. Also,

integrating the electrical contact conductance over the entire surface gives us

$$g = \int_d^\infty \frac{4}{\rho_1 + \rho_2} D_{sum} R^{\frac{1}{2}} (z - d)^{\frac{3}{2}} f(z) dz \quad (10)$$

To simplify the integration in Eq. (9) and (10), the equations are written in terms of the normal probability distribution $\varphi(x)$ function

$$\varphi(x) = \frac{1}{\sqrt{2\pi}} e^{-\frac{x^2}{2}} \quad (11)$$

The height variables are scaled for convenience using σ_{sum} and after some mathematical manipulation, we finally get

$$p = \frac{4}{3} E_{eq} D_{sum} R^{\frac{1}{2}} \sigma_{sum}^{\frac{3}{2}} F_1(\frac{d}{\sigma_z}) \quad (12)$$

$$g = \frac{4}{\rho_1 + \rho_2} D_{sum} R^{\frac{1}{2}} \sigma_{sum}^{\frac{3}{2}} F_1(\frac{d}{\sigma_z}) \quad (13)$$

$$r = \frac{1}{g} \quad (14)$$

Where, r is the contact resistance and

$$F_n(t) = \int_t^\infty (x - t)^n \varphi(x) dx \quad (15)$$

Where, the function in Eq. (15) is evaluated by expressing it in terms of parabolic cylinder functions $U(a,t)$ [38] as

$$F_n(t) = \frac{n!}{\sqrt{2\pi}} \frac{U(n + \frac{1}{2}, t)}{t^{\frac{n+1}{2}}} \quad (16)$$

It is clear from Eq. (12), (13) and (14) that the compression pressure and the contact resistance are a function of the material properties in E_{eq} and the statistics of the mating surfaces in D_{sum} , R and σ_{sum} . Since the material properties are known we are left to evaluate the mentioned statistical parameter in order to predict the interfacial resistance of the mating surfaces.

The material properties of the MPL and CL are reported in Table 2. Since this is a layered contact problem, and the materials forming the interface are

very thin, we approximate the young's modulus with that of the GDL, since it is the GDL that plays the role of a backing material for the interface in consideration.

Properties	Material	Value	Units
Young's Modulus ^[36]	GDL	10000	MPa
Electrical conductivity ^[37] (through plane)	MPL	300	S.m ⁻¹
Electrical conductivity ^[37] (through plane)	CL	200	S.m ⁻¹

Table 2: Material properties of the backing and interface materials

In order to evaluate the parameters R , σ_{sum} and D_{sum} , we do the following statistical manipulation developed by Nayak [21]. Consider $Z(x)$, the analytical function derived in Eq. (2), represents a continuous surface profile. At this juncture, we approximate the surface to be isotropic. The Auto-Correlation Function (A.C.F) $A(x)$, is defined as

$$A(x) = \lim_{L \rightarrow \infty} \left[\frac{1}{2L} \left(\int_0^L z(x) \cdot z(x+j) dj \right) \right] \quad (17)$$

Where, L is the length of the profile

The Power Spectral Density Function (P.S.D.F) $\Phi(k)$, is defined as the Fourier transform of the A.C.F as

$$\phi(k) = \frac{1}{2\pi} \left[\int_{-\infty}^{\infty} A(x) e^{-j2\pi k x} dx \right] \quad (18)$$

Where, k is the wave number of the spectral component that constitutes the surface profile.

The Spectral Moments (m_0 , m_2 and m_4) of the P.S.D are defined as

$$m_i = \int_{-\infty}^{\infty} k^i \phi(k) dk \quad (i = 0, 2, 4) \quad (19)$$

The Bandwidth Parameter α , introduced by Nayak, which depends on the shape and the extent of the spectrum of the roughness profile, is defined as

$$\alpha = \frac{m_0 m_4}{m_2^2} \quad (20)$$

Nayak showed that the parameters R , σ_{sum} and D_{sum} can be expressed solely as a function of the spectral moments (m_0 , m_2 and m_4) and the bandwidth parameter α . The corresponding relation are shown below

$$R = \frac{3}{8} \left(\frac{\pi}{m_4} \right)^{\frac{1}{2}} \quad (21)$$

$$\sigma_{sum} = \left[\left(1 - \frac{0.8968}{\alpha} \right) m_0 \right]^{\frac{1}{2}} \quad (22)$$

$$D_{sum} = \frac{1}{6\pi\sqrt{3}} \left(\frac{m_4}{m_2} \right) \quad (23)$$

It was mentioned at the beginning of the formulation that the contact between a smooth and a rough surface is considered. O'Callaghan and Cameron [18, 23] that the contact of two rough surfaces is negligibly different from the contact of a smooth and an equivalent rough surface. Hence, given the values of m_0 , m_2 and m_4 of the two rough surfaces in consideration i.e. the CL and MPL surfaces, the corresponding values for the equivalent rough surface are computed as the respective sums, i.e.

$$(m_0)_{eq} = (m_0)_{MPL} + (m_0)_{CL} \quad (24)$$

$$(m_2)_{eq} = (m_2)_{MPL} + (m_2)_{CL} \quad (25)$$

$$(m_4)_{eq} = (m_4)_{MPL} + (m_4)_{CL} \quad (26)$$

And,

$$(\alpha)_{eq} = \frac{(m_0)_{eq} (m_4)_{eq}}{(m_2)_{eq}^2} \quad (27)$$

Once the equivalent values of m_0 , m_2 , m_4 and α are calculated, these are inputted into Eq. (21), (22) and (23) to obtain the statistical parameters R , σ_{sum} and D_{sum} . Since the compression pressure applied to the fuel cell is known, the surface separation d can be evaluated from Eq. (12). Knowing d the conductance g and hence the MPL/CL interfacial resistance r is evaluated from Eq. (13) and (14).

4. Results and Discussion

Optical profilometry results indicate that both MPL and CL surfaces exhibit a high degree of roughness with structures such as high hills, large valleys and deep cracks on the surface (Figure 12 and 13). Since the use of a single roughness parameter can lead to dubious conclusions, a set of 3 roughness parameters were used to compare surface roughness of MPL and CL surfaces [28]. Optical profilometry roughness parameters (λ_a , λ_g and λ_t) which are described in full detail in British Standards [30] suggest that MPL surface exhibits a higher degree of roughness compared to CL surface (Table 3).

SEM images show that there are big differences between surface cracks on MPL and CL surfaces in terms of their orientation, size, shape, depth and density (Figure 14). Cracks on the CL surface are in the shape of thin ribbons that are aligned with respect to each other. There is no significant variance in the crack width which is around 15 μm at the crack center. The cracks extend through the entire MEA thickness as the SEM images, height values in the profilometry data, and examinations of the surface with the naked eye indicate. Surface crack density is calculated to be around 3.4 %. On the contrary, cracks on the MPL surface are randomly oriented with larger and variable width which can be as large as 60 μm . Holes and dents with diameter on the order of 100 μm are also present on the MPL surface. Frequency of these holes on the MPL surface is variable. The holes are observed to be very closely spaced on certain regions of the surface, and they are very rare or not present at all on some other regions. Depending on the frequency of these holes, the cracks density was found to vary greatly from 2.8 % to 8.9 % percent. Although optical profilometry data regarding crack depth is missing to a large extent for MPL, data obtained from few points on the crack base indicate that crack depth is as large as the MPL thickness. In the SEM images, fibers belonging to the GDL are also visible through some of the cracks on the MPL surface. These observations form strong evidence that cracks on the MPL surface (at least some of them) extend through the entire MPL thickness, till GDL. In the previous modeling studies conducted to determine the influence of MPL on water balance [31, 32, 33], MPL was considered to be a purely porous medium and the effect of macro-cracks and holes in the MPL structure were not taken into account. Although the micro-sized pores of MPL are taught to help water removal from the cathode

catalyst layer by acting like a wick [34], existence of the macro-cracks and holes in the MPL structure may avoid proper functioning of MPL by reducing capillary pressure forces. Moreover, the regions on the MPL/CL interface where a cracked and a non-cracked surface come up against each other may act as water accumulation sites and reduce the overall fuel cell performance.

It is quite clear that the contact resistance of the MPL/CL interface is a strong function of the material properties of the backing GDL layer and the statistical parameters of the surfaces the primary one being their roughness. Figure 10 shows the variation of contact resistance as a function on the applied compression pressure. Under normal operating conditions i.e. at a compressive pressure of 1.5 MPa, the model predicts the MPL/CL contact resistance to be $\sim 1.8 \text{ m}\Omega\cdot\text{cm}^2$ considering only one CL/MPL interface, which agrees well with the experimental results [35]. To gauge the effect of MPL and CL surface roughness on the contact resistance, cases with 50% higher and lower relative CL and MPL average roughness were simulated and are shown in figure 10. It was observed that by lowering the MPL and CL average roughness by 50%, as much as 40% drop in contact resistance can be achieved. This high drop can be explained with the fact that at lower roughness of the surfaces, the number of contact points drastically increase thereby facilitating a much higher amount of electron flow across the MPL/CL interface at the micro-level. It was also observed that the MPL surface roughness has a much greater effect on the MPL/CL interfacial resistance as its roughness is higher when compared to the CL roughness.

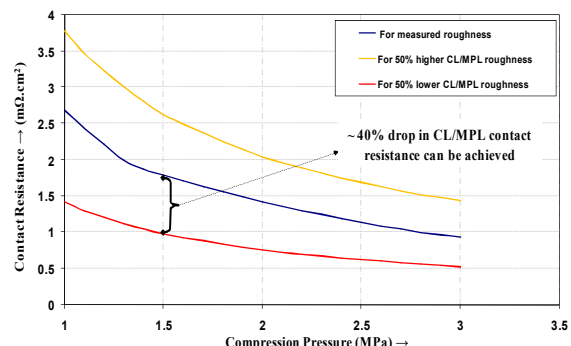


Figure 10. MPL/CL contact resistance v/s Fuel cell compression pressure

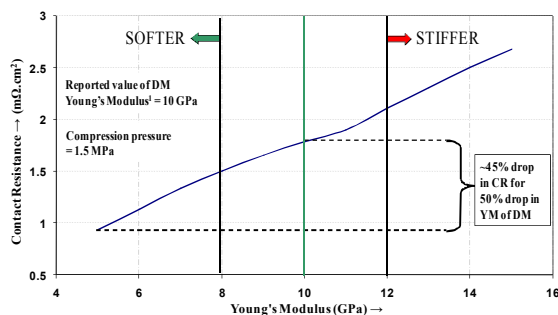


Figure 11. MPL/CL contact resistance v/s Young's modulus of backing GDL layer

As mentioned earlier, the material property i.e. the young's modulus of the backing GDL layer has a crucial impact on the MPL/CL interfacial resistance. It is shown in figure 11, via simulation that, a 50% drop in the young's modulus from its

current measured value results in almost 45% drop in the MPL/CL contact resistance. The reason for such a high correlation of contact resistance with the material property of the backing layer is that as the elastic modulus is lowered, the backing material becomes relatively softer providing more flexibility to the MPL and CL to deform. This locally enhances the MPL/CL warping ability thereby generating more mating points as the surfaces deform to improve the contact and hence lowering the interfacial resistance.

Because MPL surface exhibits a higher degree of roughness with cracks of higher depth compared to CL surface the morphology of the MPL/CL interfacial structure, interfacial losses and local transport at the interface will be dominated by the MPL surface morphology. Hence tailoring the MPL surface for improved surface characteristics is expected to enhance the performance of the fuel cell.

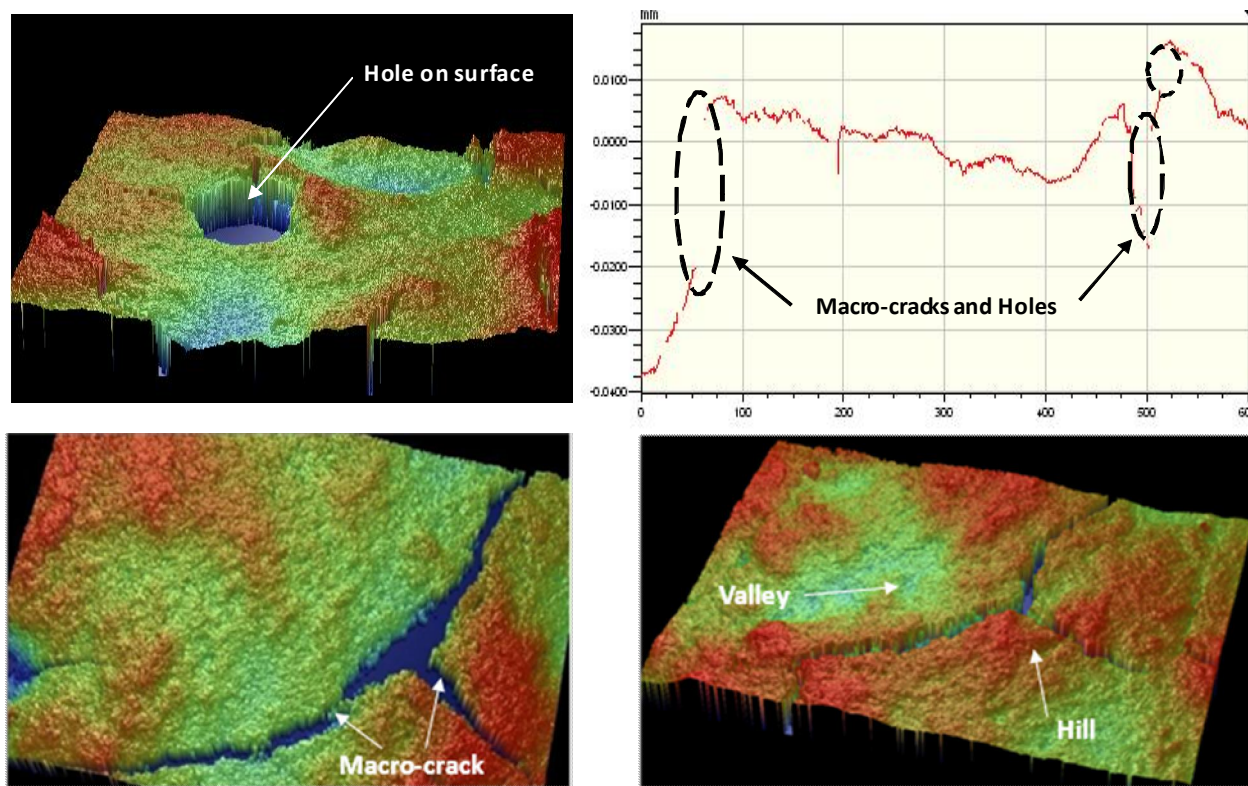


Figure 12. Representative 3D images and surface profiles of MPL Side of SGL 10BB obtained using optical profilometry

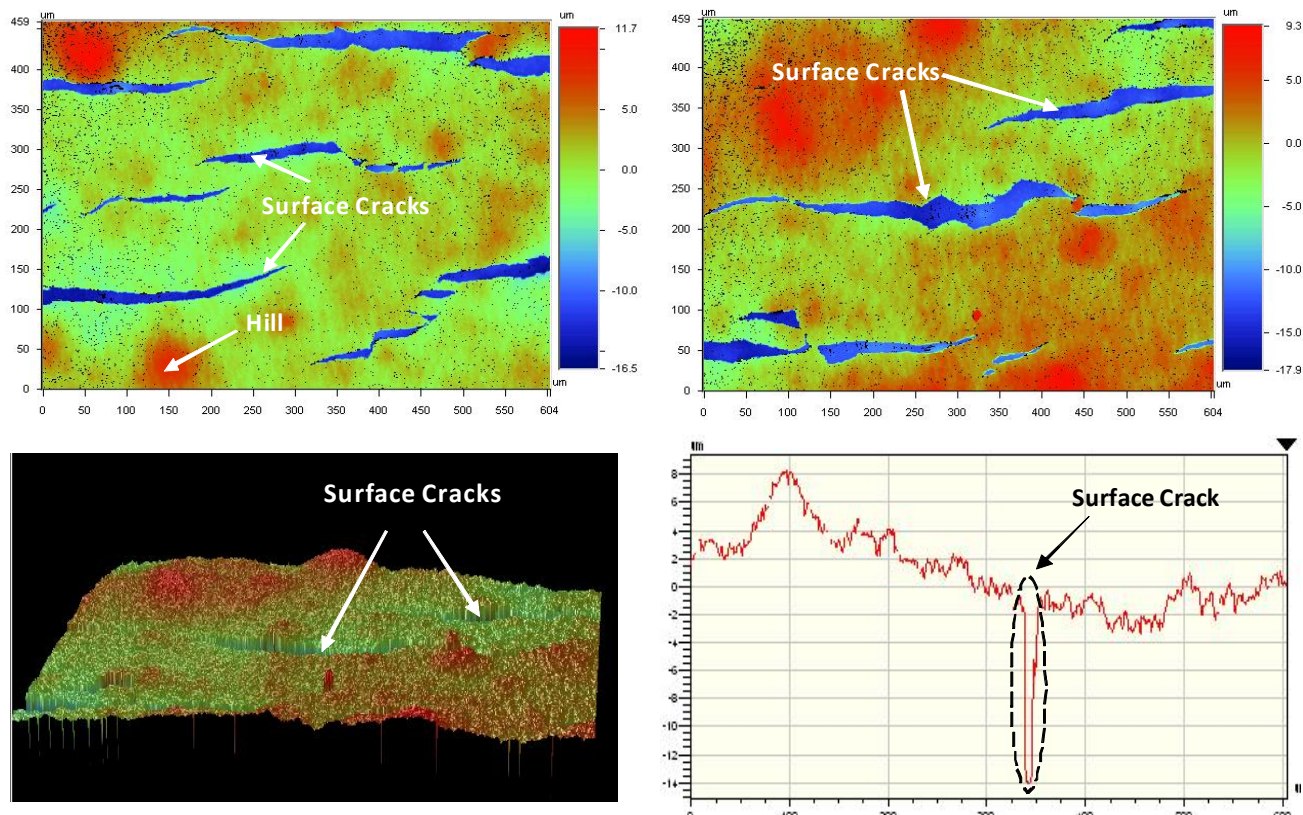


Figure 13. Representative 2D and 3D images, and surface profile of cracked CL obtained using optical profilometry images.

Sample	$\lambda_a(\mu\text{m})$	$\lambda_g(\mu\text{m})$	$\lambda_t(\mu\text{m})$
MPL	5.35 ± 1.96	7.39 ± 3.20	68.32 ± 19.95
Cracked CL	2.19 ± 0.20	3.63 ± 0.21	26.56 ± 3.19

Table 3. Surface roughness data of MPL and CL samples (arithmetic mean values \pm standard deviation of 18 measurements)

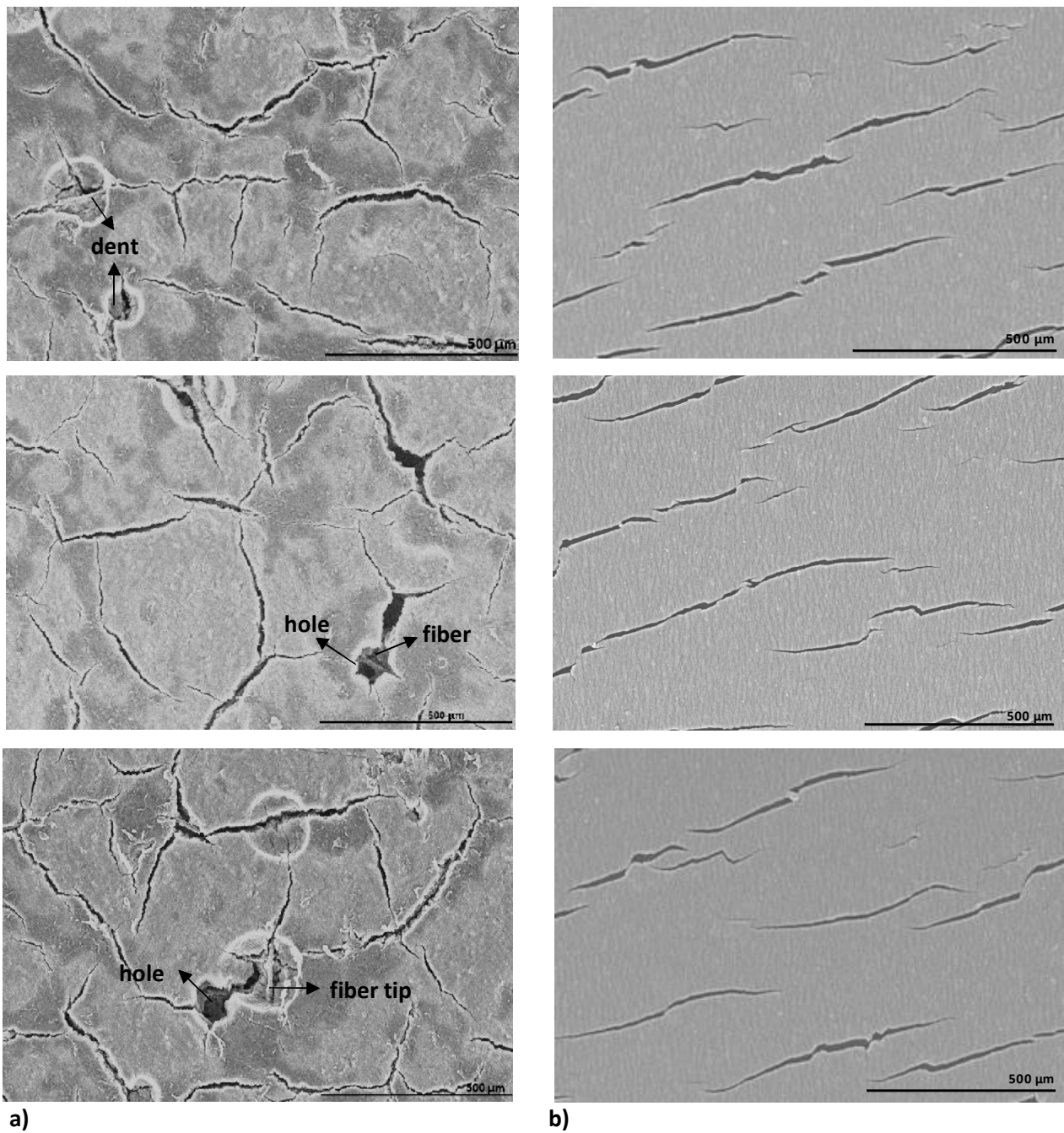


Figure 14. Representative SEM images of a) MPL side of SGL 10BB, b) Cracked CL.

5. CONCLUSION

Impact of MPL and CL surface characteristics, which determine the morphology and structure of the MPL/CL interface, on the overall fuel cell performance is demonstrated.

MPL and cracked CL surfaces are characterized using optical profilometry and SEM. MPL surface is found to exhibit a higher degree of roughness compared to CL surface. Macro-cracks are observed on both surfaces. Macro-cracks on MPL surface are found to have larger size, higher depth and more variable characteristics compared those on CL surface.

Modeling results show that these topological characteristics of the mating surfaces have a significant effect on the contact resistance. Simulations of the interface indicate that a decrease in MPL and CL roughness by 50%, results in a 40% drop in contact resistance. The model also predicts that MPL surface roughness has a greater effect on the MPL/CL interfacial contact resistance.

Highly rough surface nature of MPL and CL and the existence of macro-cracks are also expected to significantly increase the mass transport losses by interfering with the water transport through the MPL/CL interface, forming sites of flooding at the interfacial gaps and preventing MPL from functioning properly.

The interface model also shows that the material properties of the fuel cell components have a significant impact on the interfacial resistance. A 50% drop in GDL's young's modulus from its current measured value results in almost a 45% drop in the MPL/CL contact resistance.

MPL surface has a rougher nature and cracks of higher depth compared to CL surface. Thus MPL surface characteristics will dominate the MPL/CL interfacial structure, the local transport through it and interfacial losses. Altering the MPL surface to obtain a layer with superior surface characteristics is expected to improve the performance of the fuel cell.

NOTATION

<i>z</i>	Height of asperity, mm
<i>p</i>	Compression pressure, MPa
<i>P</i>	Compression Load, kg
<i>d</i>	Surface mean plane separation, mm
<i>R</i>	Radius, mm
<i>E_i</i>	Young's Modulus, (<i>i</i> = 1, 2), MPa
<i>v_i</i>	Poisson's Ratio, (<i>i</i> = 1, 2), Unitless
<i>ρ_i</i>	Resistivity, (<i>i</i> = 1, 2), Ω.mm
<i>σ</i>	Standard deviation, mm
<i>D</i>	Density of summits on the surface, mm ⁻²
<i>g</i>	Conductance, mΩ ⁻¹ .cm ⁻²
<i>r</i>	Resistance, mΩ.cm ²
<i>λ</i>	Roughness, μm

Subscripts

<i>eq</i>	Equivalent
<i>c</i>	Contact (single)
<i>sum</i>	Summit
<i>a</i>	Average
<i>q</i>	Root mean square
<i>t</i>	Maximum height of the surface

REFERENCES

1. M. Eikerling, *J Electrochem. Soc.*, 153 (3), E58-E70 (2006).
2. P. Berg, K. Promislow, *J. Electrochem. Soc.*, 151 (3), A341-A353 (2004).
3. T.A. Zawodzinski, C. Derouin, S. Radzinski, R.J. Sherman, T. van Smith, T.E. Springer, S. Gottesfeld, *J. Electrochem. Soc.*, 140(4), 1041-1047 (1993).
4. V. Gurau, T.A. Zawodzinski, J.A. Mann, *J. Fuel Cell Sci. Technol.* 5, 021009 (2008)
5. L. You, H. Liu, *Int. J. Heat Mass Transfer* 45 (2002), pp. 2277-2287.
6. C. Marr, X. Li, *J. Power Sour.* 77 (1999), pp. 17-27
7. D.M. Bernardi, M.W. Verbrugge, *AIChE J.* 37 (8) (1991) 1151.
8. T.E. Springer, M.S. Wilson, S. Gottesfeld, *J. Electrochem. Soc.* 140 (12) (1993) 3513.
9. J.H. Nam and M. Kaviany, *Int. J. Heat Mass Transfer* 46 (2003), pp. 4595-4611.
10. U. Pasaogullari and C.-Y. Wang, *Electrochim. Acta* 49 (2004), pp. 4359-4369.
11. A.Z. Weber and J. Newman, *J. Electrochem. Soc.*, 152 (4), A677-A688 (2005).
12. Z. Qi and A. Kaufman, *J. Power Sources* 109 (2002), pp. 38-46.
13. G. Lin and T.V. Nguyen, *J. Electrochem. Soc.* 153 (2006), pp. A372-A382.
14. U. Pasaogullari, C.-Y. Wang and K.S. Chen, *J. Electrochem. Soc.* 152 (2005), pp. A1574-A1582.
15. G.J.M. Janssen and M.L.J. Overvelde, *J. Power Sources* 101 (2001), pp. 117-125.
16. Y. Zhou, G. Lin, A.J. Shih, S.J. Hu, *Journal of Power Sources*, 163 (2007) 777-783.
17. Z. Wu, Y. Zhou, G. Lin, S. Wang, S.J. Hu, *Journal of Power Sources* 182 (2008) 265-269
18. J. I. McCool, *Wear*, 107 (1986) 37-60
19. J. A. Greenwood and J. W. P Williamson, *Proc. R. Soc. London, Ser. A*, 295 (1966) 300-319.
20. J. A. Greenwood, *Wear*, 262 (2007) 225-227.
21. P. R. Nayak, *J. Lubr. Tech.*, 93 (1971) 398-407.
22. A.W. Bush, R.D. Gibson and T.R. Thomas, *Wear*, 35 (1975) 87 - 111.
23. M. O'Callaghan and M. A. Cameron, *Wear*, 36 (1976) 79-97.
24. L. Chang, *Journal of Engineering Tribology, Proc. IMechE Vol. 223 Part J*, In Press.
25. R. Holm, 'Electrical Contacts Handbook', *Springer-Verlag*, 1958
26. R. Chopra, F. Podczeck, J.M Newton, G. Alderborn, *Part. Part. Syst. Charac.* 19, 277-283 (2002).
27. P. Seitavuopio, The roughness and imaging characterization of different pharmaceutical surfaces. *Helsinki: Helsinki University Printing House* (2006).
28. F. Podczeck, Particle-particle Adhesion in Pharmaceutical Powder Handling. *London: Imperial College Press* (1998).
29. D. Faith, C.J. Horsfield, *J. Mater. Sci.* 41 (2006) 3973-3977.
30. British Standard 1134: Method for the Assessment of Surface Texture, *British Standard Institution, London*, 1972.
31. J.H. Nam and M. Kaviany, *Int. J. Heat Mass Transfer*, 46 (24), 4595-4611 (2003).
32. U. Pasaogullari and C.-Y. Wang, *Electrochim. Acta*, 49 (25), 4359-4369 (2004).
33. A.Z. Weber and J. Newman, *J. Electrochem. Soc.*, 152 (4), A677-A688 (2005).
34. M. Mathias, J. Roth, J. Fleming and W. Lehnert, Diffusion Media Materials and Characterization. In: W. Vielstich, A. Lamm and H. Gasteiger, Editors, *Handbook of Fuel Cells—Fundamentals, Technology and Applications. Vol. 3, John Wiley & Sons, New York* (2003).
35. R. Makharia, M.F. Mathias and D.R. Baker, *J. Electrochem. Soc.*, 152(5) A970-A977 (2005)
36. A. Kusoglu, A.M. Karlsson a, M.H. Santare, S. Cleghorn, W.B. Johnson, *Journal of Power Sources* 161 (2006) 987-996
37. S. Kim, M. Khandelwal, C. Chacko and M.M Mench, 2008, *Journal of the Electrochemical Society*, 156 pp. B99-B108
38. M. Abramowitz and I.A. Stegun, *Handbook of Mathematical Functions, Vol. 55, Applied Mathematics Series, U.S. Department of Commerce, Springfield, VA*, 1964